Electroluminescence in Unipolar-Doped In$_{0.53}$Ga$_{0.47}$As/AlAs Resonant-Tunneling Diodes: A Competition between Interband Tunneling and Impact Ionization

E.R. Brown,[1,*] W.-D. Zhang,[1] T.A. Growden,[2] P. Fakhimi,[3] and P.R. Berger[3]

[1]*Department of Physics, Wright State University, 3640 Colonel Glenn Hwy, Dayton, Ohio 45435, USA*

[2]*U.S. Naval Research Laboratory, Washington, DC, 20375, USA*

[3]*Department of Electrical and Computer Engineering, Ohio State University, Columbus, Ohio 43210, USA*

We measure and analyze the light emission from a room-temperature *n*-type unipolar-doped In$_{0.53}$Ga$_{0.47}$As/AlAs double-barrier resonant-tunneling diode (RTD) that occurs just above the In$_{0.53}$Ga$_{0.47}$As band edge and peaks around 1631 nm. The emission is attributed to electron-hole recombination emission made possible by holes generated in the high-field region on the collector side of the device by interband tunneling and impact ionization, which contribute comparable hole densities, according to our analysis. Although the external quantum efficiency (EQE) in our experimental configuration is rather low ($\approx 2 \times 10^{-5}$ at 3.0-V bias), limited by suboptimal output coupling, the internal quantum efficiency (IQE) is much higher ($\approx 6\%$ at 3.0-V bias), as derived from the experimental EQE and a radiometric analysis. To check this value and better understand the transport physics, we also carry out an independent estimate of the IQE using a combined interband-tunneling impact-ionization transport model, which yields an IQE of 10% at 3.0-V bias. The satisfactory agreement of theory with experimental data suggests that a RTD designed for better hole transport and superior optical coupling could become a useful light-emitting device, while retaining the intrinsic functionality of high-speed negative differential resistance, and all without the need for resistive *p*-type doping.

I. INTRODUCTION

Interband tunneling has been an important aspect of electron transport in crystalline solids since the seminal paper by Zener in 1934 [1]. However, a useful demonstration in electronic devices had to wait for the development of semiconductor technology in the early 1950s, with the demonstration of controllable "breakdown" in back-biased Ge *p-n* Zener diodes. Then, in the same decade, the interband tunneling effect was accentuated to make a device with negative differential resistance at room temperature, the Esaki tunnel diode [2], which ultimately led to the Physics Nobel Prize in 1973. More recently, interband tunneling has been revived with lateral-tunneling field-effect transistors (TFETs) as a means of overcoming the fundamental lower limit (60 mV/dec) of turn-on voltage in Si MOS devices [3–6]. It has also been utilized to make highly sensitive radio-frequency rectifiers in *p-n*-doped type-III (broken gap) III-V heterostructures [7] and highly efficient tandem heterojunction solar cells [8]. The primary purpose of this paper is to demonstrate that interband tunneling may also be useful for

n-type unipolar-doped photonic sources via electroluminescence at room temperature. Double-barrier resonant-tunneling diodes (RTDs) have already proven their utility as room-temperature optical detectors in optoelectronic integrated circuits [9], but not yet as practical photonic sources. A key issue is their internal quantum efficiency (IQE).

A secondary purpose of this paper is to propose that the holes created on the collector side by interband tunneling or impact ionization can transfer efficiently to the emitter side by *intraband* tunneling through a straddling-gap (type-*I*-offset) double-barrier structure. In the present case, the structure is a "garden-variety" In$_{0.53}$Ga$_{0.47}$As/AlAs double-barrier RTD of the type normally used for high-speed electron resonant-tunneling devices. Hole resonant tunneling is known to occur in such RTD structures, when they are *p*-type doped [10], but is significantly more complicated than electron resonant tunneling because of light-hole–heavy-hole mixing effects. However, we emphasize that the resonant tunneling of holes is not required for the IQE results presented here, rather, just significantly high overall hole-transmission probability. Hence, our results suggest that both electron and hole intraband tunneling are occurring simultaneously and efficiently through the same double-barrier structure. More

*elliott.brown@wright.edu

importantly, both tunneling mechanisms are strong enough to enable a light-emission mechanism that is surprisingly efficient, considering there is no *p*-type doping in the structure.

We have already observed room-temperature electroluminescence from *n*-type unipolar GaN/AlN [11] and $In_{0.53}Ga_{0.47}As$/AlAs [12] double-barrier RTDs via emission from the sidewalls of mesa-isolated devices. Both were attributed qualitatively to hole generation by interband tunneling in the device structure, although proof was lacking because of unknown quantum efficiencies and the lack of a comparison with the other possible source of holes: impact ionization. Here, we report on band-edge emission from a separate unipolar $In_{0.53}Ga_{0.47}As$/AlAs RTD designed for partial vertical emission, and thus, take the analysis an important step further by deriving the IQE from experimental measurements and calculations using two independent methods. The first method is based on a direct measurement of the experimental external quantum efficiency (EQE) and a radiometric calculation of the optical coupling factor. The second is based on a holistic charge-transport computation of the available hole current by both interband tunneling and impact ionization on the collector side and radiative recombination on both sides. Interband tunneling and impact ionization are shown to yield comparable available hole currents with impact ionization exceeding interband tunneling at modest bias (around the peak voltage of the RTD) and interband tunneling dominating at the highest bias tested where the strongest and most-efficient light emission occurs.

II. DEVICE DESIGN AND EXPERIMENTAL CHARACTERIZATION

The device demonstrated here is a garden-variety $In_{0.53}Ga_{0.47}As$ RTD, designed for electrical negative differential resistance (NDR), and grown by molecular-beam epitaxy on a semi-insulating InP substrate and having the growth stack and *n*-type doping profile shown in Fig. 1(a). It is similar in design to state-of-the-art RTDs, which, in recent years, have extended the maximum frequency of solid-state self-oscillators above 1.0 THz [13], continuing to advance RTDs as the fastest room-temperature solid-state oscillators since 1991 [14]. The active region is comprised of two unintentionally doped (UID) AlAs barriers (thickness ≈ 1.7 nm, or 6 monolayers) separated by an undoped $In_{0.53}Ga_{0.47}As$ quantum-well (width $= 5.0$ nm) layer, such that an electron quasibound level, $U_{1,e}$, occurs in the quantum well at an energy level of about 0.193 eV above the $In_{0.53}Ga_{0.47}As$ conduction-band edge at zero bias. As described in Sec. IV A, the high $U_{1,e}$ level is due, in part, to the narrow well and, in part, to the low electron effective mass at the conduction-band edge ($m^*_e = 0.042$ m_e), where m_e is the vacuum electron mass. Immediately outside the double-barrier structure are 2-nm undoped spacer layers and then low *n*-doped ($N_d = 1 \times 10^{17}$ cm^{-3}) layers with thicknesses of 65 and 10 nm on the top and bottom sides, respectively. Outside of the *n*-doped regions are n^+-doped ($N_d = 2 \times 10^{18}$ cm^{-3}) contact layers to which electrical ohmic contacts are made. The structure is designed for positive bias on the top (collector) side, which tends to deplete the top 65-nm *n*-type region and create a low collector-side capacitance
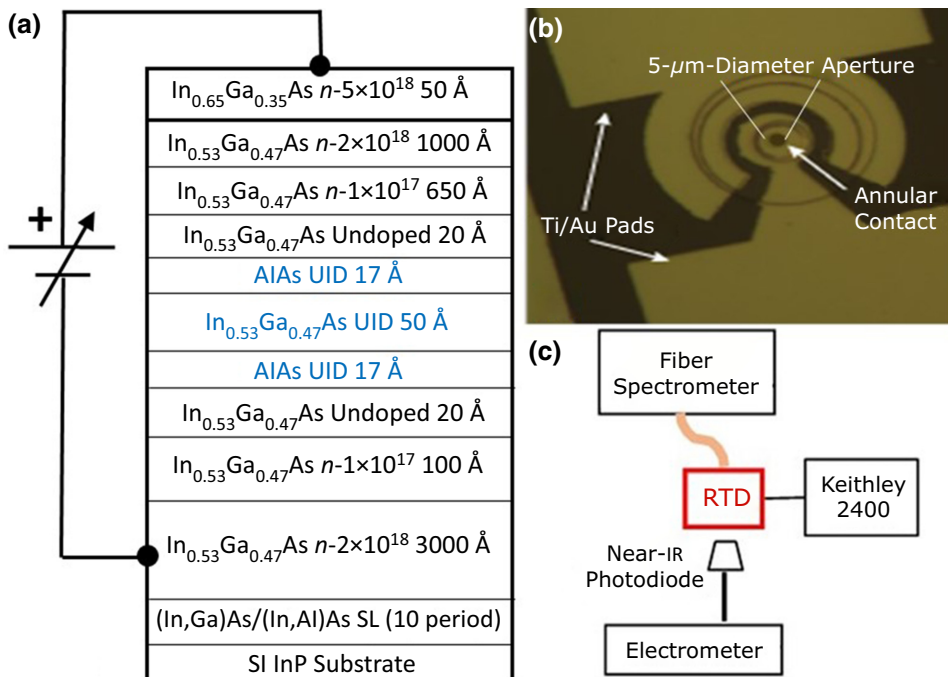

FIG. 1. (a) MBE-growth stack. (b) Microphotograph of fabricated device with vertical emission aperture. (c) Experimental setup for measurement of electrical and optical characteristics.

for high-speed device operation in oscillators and switches. Because of the large $U_{1,e}$, a relatively high bias voltage of $V_B \sim 2.0$ V is required to achieve the peak condition of resonant (intraband) tunneling. As described below, the large bias and depleted collector layer are important factors in promoting the cross-gap electroluminescence.

Working devices are fabricated as 15-μm-diameter circular vertical mesas including a top annular ohmic contact with a 5-μm-diameter pinhole in the center to couple out light vertically for accurate free-space power measurements. A microphotograph of the fabricated annular-contact structure is shown in Fig. 1(b). For device characterization, the setup shown in Fig. 1(c) is used, consisting of a precision I-V probe station, a near-IR calibrated photodetector, and a near-IR overmoded-fiber spectrometer. The ambient temperature is $T \approx 300$ K. The detector is a large-area (3-mm-diameter) Ge photodiode with a spectral response between 800 and 1800 nm and a peak responsivity of $\mathfrak{R} \approx 0.85$ A/W at a wavelength of 1550 nm. It is optically coupled through free space with the photodiode located as close as is practical (approximately 3 mm, limited by packaging issues) to the double-barrier RTD. Its output is dc coupled to a solid-state electrometer with a current noise floor of about 1 pA. The fiber spectrometer is a room-temperature near-infrared (NIR) $In_{0.53}Ga_{0.47}As$-array-grating instrument sensitive between 880 and 1750 nm and having a programmable spectral resolution [15], which is chosen, for the present experiments, to be 0.5 nm.

Figure 2 shows the electric current-voltage (I-V) and current-density curves (left vertical axis), along with the broadband light versus voltage (L-V) curve measured for the device (right vertical axis), where L is the photodiode output current measured in units of nA. The I-V curve displays a pronounced electrical NDR region with a peak voltage of 1.8 V, a valley voltage of 2.5 V, and a current peak-to-valley current ratio (PVCR) of 10.7, which is typical for high-quality $In_{0.53}Ga_{0.47}As$ RTDs at room temperature. The terminal electric current density, J_E, is calculated from the current through division by the mesa area of 177 μm^2, which yields a peak J_E of about 26 kA/cm^2. In the NDR region, between the peak and valley, there is a chairlike structure, usually indicative of instability or self-oscillations driven by the modestly large current density here, and we make no attempt to terminate the RTD with a low enough source impedance to suppress oscillations in the present experiments. The L-V curve displays a threshold of light emission at about 1.2 V, followed by a rapid increase to a local maximum at the peak voltage of the I-V curve. In the NDR region, the L-V curve is jagged, suggesting that the light emission is affected by the electrical instability, and therefore, likely to occur in the active region of the RTD. Above the valley voltage, the light emission increases very rapidly again, reaching a maximum (for the present experiments) at 3.0 V. The L-V curve
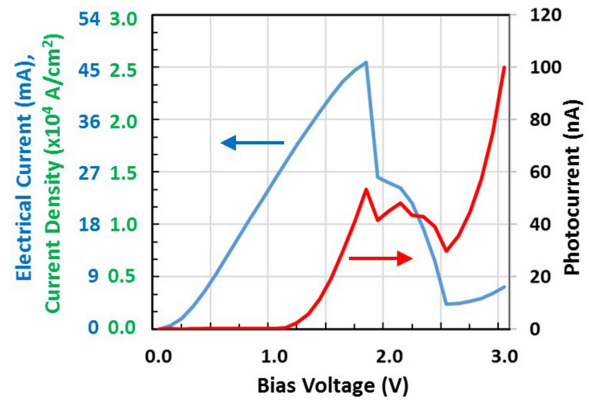

FIG. 2. Experimental I-V curve (left vertical axis) and L-V curve (right vertical axis) at 300 K.

in this region increases with bias voltage faster than the electric current, which is an important clue in the interpretation provided by our model for the electroluminescence, as described below.

The emission spectra are plotted in Figs. 3(a) (versus wavelength) and 3(b) (versus photon energy) at $V_B = 2.8$ and 3.0 V, both above the RTD valley voltage. $V_B = 3.0$ V yields the strongest and most-efficient electroluminescence performance characteristics measured on this device. For both bias voltages, the long-wavelength-emission edge is at $\lambda \approx 1680$ nm, which is just beyond the $In_{0.53}Ga_{0.47}As$ band-gap wavelength of 1661 nm (corresponding to $U_G \approx 0.747$ eV at 300 K [16]). However, the peaks for both emission spectra occur at $\lambda \approx 1631$ nm ($h\nu = hc/\lambda = 0.761$ eV, where c is the speed of light), and thus, are slightly *blueshifted* by about 14 meV relative to the band edge. This shift is well known from the following "ideal" cross-gap spectral intensity applicable to a bulk direct-band-gap semiconductor [17]:

$$S(\nu) = H(h\nu - U_G)^{1/2}\exp[-(h\nu - U_G)/k_B T], \quad (1)$$

where H is a frequency-independent constant; no cavity effects are assumed; and k_B and h are the Boltzmann and Planck constants, respectively. Equation (1) predicts a peak shift of $(1/2)k_B T = 12.9$ meV relative to U_G, which is close to our experimental shift of 14 meV. As plotted in Fig. 3(b), the experimental spectral peaks align with the ideal one to within 1 meV, which is the approximate uncertainty in photon energy around $\lambda = 1650$ nm associated with the fiber spectrometer.

In spite of the good peak agreement, there is significantly more radiation from the device than the ideal spectrum at wavelengths below the peak, as well as subband-gap radiation at wavelengths beyond the peak. As shown in Fig. 3(b), these both broaden the experimental emission to a FWHM of $\Gamma_1 = 72$ meV at $V_B = 3.0$ V ($\Delta\lambda = 148$ nm), and $\Gamma_2 = 71$ meV at $V_B = 2.8$ V. These are to be compared with $\Gamma_3 = 46.5$ meV for the ideal spectrum at $T = 300$ K
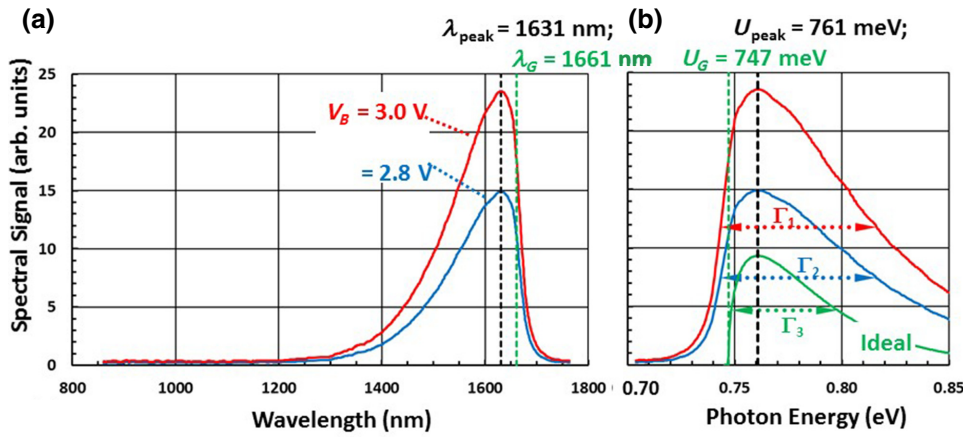
FIG. 3. (a) Experimental light-emission spectra at 300 K plotted versus wavelength for two bias voltages (2.8 and 3.0 V). Peak of both spectra occurs at about 1631 nm, and the full width at half maximum is about 148 nm. (b) Same light spectra as in (a) but plotted versus photon energy, including the ideal spectrum (offset for clarity and plotted in green) for $In_{0.53}Ga_{0.47}As$ as a direct-band-gap semiconductor.

(i.e., $\Gamma_3 = 1.8k_BT$). A likely reason for this discrepancy is alloy broadening, a mechanism caused by the random distribution of atoms in a ternary alloy, such as $In_{0.53}Ga_{0.47}As$ [17]. However, aside from the broadening effect, there is no other experimental evidence for significant nonideal emission in the range between 850 and 1750 nm. In fact, our FWHM is comparable to that of commercial 300-K p-n light-emitting diodes (LEDs) with peak emission between 1600 and 1650 nm, which is typically between $\Delta\lambda = 130$ and 150 nm [18].

III. QUANTUM EFFICIENCIES

A. Experimental EQE and radiometric estimation of IQE

Knowing experimentally that the majority of emission is occurring within the spectral range of the wideband photodiode of Fig. 1(c), we can proceed immediately with estimates of the light-emission figures of merit: the EQE and IQE. We follow the methodology outlined in Fig. 4 by first measuring the EQE. For this, we position the photodiode about 3.0 mm above the RTD pinhole and separately measure its optical responsivity to be $\Re \approx 0.85$ A/W at $\lambda = 1550$ nm. For a Ge photodiode ($U_G = 0.66$ eV; $\lambda_G = 1.88$ μm; both at 300 K), this responsivity should be approximately flat with a wavelength over the about 148-nm-FWHM 1631-nm-centered emission spectra of Fig. 3(a). The setup-dependent EQE is then estimated from

$$\text{EQE} \approx eI_{\text{ph}}/(\Re I_E h\nu), \qquad (2)$$

where I_{ph} is the photodiode dc current and I_E is the terminal RTD electric current, measured at each bias voltage of Fig. 2. The plot of EQE is shown in Fig. 5 (left vertical axis), where we see a very rapid rise with V_B, but a maximum value (at $V_B = 3.0$ V) of only about 2×10^{-5}. To extract the IQE, we use the expression

$$\text{EQE} = \eta_c \text{IQE}, \qquad (3)$$

where η_c is the optical-coupling factor [17].

To obtain an estimate of the radiometric IQE, we perform a separate calculation of η_c using radiometric methods and physical optics [19]. We treat light emission from the pinhole as Lambertian, which is consistent with emission from common LEDs. This includes the following effects, in decreasing order of importance: (1) the fraction of Lambertian radiation from the pinhole collected by the photodiode; (2) the refractive-index mismatch between $In_{0.53}Ga_{0.47}As$ ($n \approx 3.4$ at 1550 nm) and air; (3) the reduction in external-to-internal radiative power associated with the pinhole-to-RTD area ratio; and (4) the polarization-dependent transmittance between $In_{0.53}Ga_{0.47}As$ and air, averaged over the angle between $\theta = 0$ and the angle of total internal reflection ($\theta \approx 17°$). The net result is $\eta_c \approx 3.4 \times 10^{-4}$. This might seem small, but one must remember that, in the present mesa-isolated device, a large fraction of the radiation propagates either through the mesa sidewalls or into the InP substrate, where it is trapped by total internal reflection or transmitted out the chip sidewalls. Lacking the half-ball lens coupling and parabolic mirrors or external reflecting "cups," as commonly used in efficient LEDs, the vast majority of internal radiation
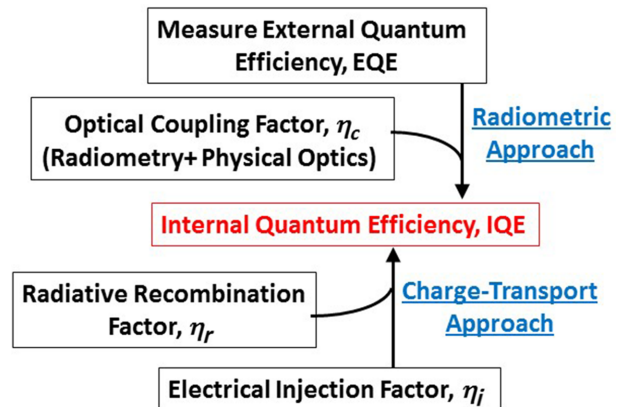

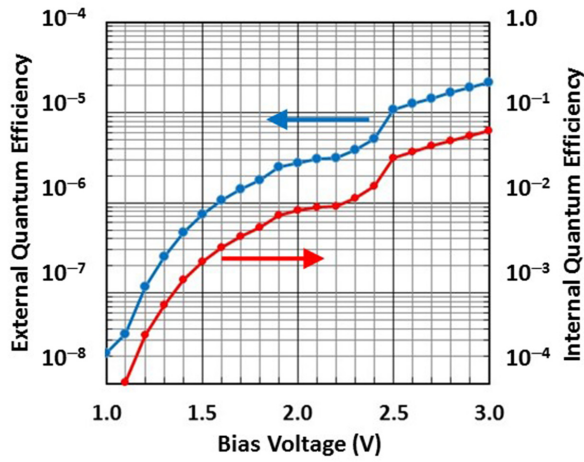FIG. 4. Methodology for estimating IQE by two separate approaches.

FIG. 5. EQE is obtained directly from experiments (left vertical axis). Internal quantum efficiency is calculated using the radiometric approach of Fig. 4 (right vertical axis).

is practically unobservable in our experiments. Given this value of η_c, we obtain the curve of IQE plotted in Fig. 5 (right vertical axis). The maximum value of IQE (again at $V_B = 3.0$ V) is about 6%, as reported last year [20].

B. Independent estimate of IQE

1. Electroluminescence model

The experimental results and physical reasoning lead to a qualitative model for the high-bias electroluminescence, as shown in the schematic diagram of Fig. 6, in which charge transport is assumed to occur along the z axis. It assumes that electron-hole pairs are generated in the high-electric-field ($E \gg 0$) region on the collector side by either interband tunneling (G_{IT}) or impact ionization (G_{II}), with the total generation rate (number of holes per unit volume time) represented by $G_{tot} = G_{IT} + G_{II}$, both a function of z. Then the holes transport either to the emitter side by tunneling through the double-barrier structure or to the quasi-neutral region ($E \approx 0$) of the collector side by diffusion. The former mechanism contributes to the electric hole current density $J_{P,E}$ and the latter to $J_{P,C}$. After transport, the holes recombine with free electrons that are abundant in these regions because of the heavy n-type doping ($N_D = 2 \times 10^{18}$ cm^{-3}). Recombination is assumed to be either cross-gap radiative, as represented in Fig. 6 by rates $R_{R,E}$ and $R_{R,C}$, or nonradiative, as defined by $R_{N,E}$ and $R_{N,C}$. Being a direct-band-gap semiconductor, In$_{0.53}$Ga$_{0.47}$As supports a large R_R without the involvement of phonons and a large R_N by Auger recombination in heavily doped (n^+) regions. All of these mechanisms and assumptions are described further in Appendix B, where they are used to support our charge-transport-based estimate of the light-emission performance.
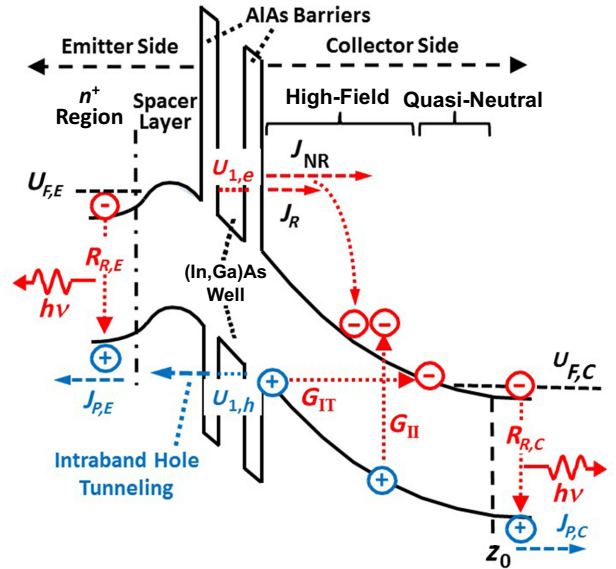

FIG. 6. Energy diagram showing a qualitative model for electron-hole generation by interband tunneling, G_{IT}, or by impact ionization, G_{II}, on the collector side of the In$_{0.53}$Ga$_{0.47}$As/AlAs RTD and radiative recombination at either the emitter side or in the quasi-neutral or n^+ regions on the collector side.

Figure 6 displays qualitatively an important aspect of our structure, which is a nonuniform electric field across the high-field region on the collector side. This is caused by n^- doping ($N_D = 1 \times 10^{17}$ cm^{-3}) on this side, which is typically done in RTDs designed for electronic applications to reduce the voltage drop across the collector side without introducing deleterious scattering of tunneling electrons by ionized impurities. This is in contrast to the intrinsic condition typically practiced in Zener diodes and p-i-n impact-ionization devices. It also causes the electric field to be highest near the double-barrier structure on the collector side and significantly smaller approaching the quasi-neutral region. As we will see further below, this tends to promote the strongest G_{IT} near the double-barrier structure and the strongest G_{II} near the quasi-neutral region, where the kinetic energy of electrons transmitted through the double-barrier structure is the highest. The transmission mechanism can be either by elastic resonant tunneling through the quasibound electron level, $U_{1,e}$, and represented by J_R, or by inelastic tunneling through the double-barrier structure and represented by J_{NR}. Our model assumes that both can contribute to impact ionization in a manner that will be described below.

Another essential aspect of our model is the transport of holes once generated. Even though the high-field region on the collector side is n^- doped, it is mostly depleted of free electrons under high bias. Hence, the majority of holes should experience insignificant radiative and nonradiative recombination in the depletion region because of the

sparsity of stationary free electrons there and the low concentration of traps and recombination centers expected in high-quality epitaxial $In_{0.53}Ga_{0.47}As$. So, the holes should either drift ("uphill" in Fig. 6) towards the double-barrier structure or diffuse ("downhill" in Fig. 6) towards the quasi-neutral region on the collector side. The drifting holes will encounter the double-barrier structure, which, as we will discuss later, can support resonant tunneling of holes and electrons. By contrast, the diffusing holes encounter no such barrier. The balance between drift and diffusion of the holes is an important and complicated aspect of our RTD light emitter, but we formulate the charge-transport analysis in such a way that we can extract the most-important light-emission metric, the IQE, without knowing this balance.

2. Charge-transport calculation

To obtain a charge-transport estimate of the IQE, we derive in Appendix B the following expression applicable to electroluminescence in any solid-state device:

$$IQE = \eta_r \eta_i = \eta_r e \Phi_{G,\text{tot}} / J_T, \qquad (4)$$

where η_r is the radiative recombination factor, η_i is the electrical injection factor, $\Phi_{G,\text{tot}}$ is the total *available* hole flux, and J_T is the terminal electric current density. Since the radiometric approach to IQE does not have a direct dependence on charge transport, Eq. (4) also serves as an independent test of our electroluminescence model of Fig. 6. Given the symmetric n^+-doping profile in the recombination regions, it is shown in Appendix B that

$$\eta_r = Bnp/(Bnp + Cn^2p) = (1 + Cn/B)^{-1}, \qquad (5)$$

where B is the bimolecular recombination coefficient, and C is the three-particle (electron-electron-hole) Auger coefficient in these regions. In the n^+ regions, $n \approx N_D = 2 \times 10^{18}$ cm^{-3} for which $B \approx 1.4 \times 10^{-10}$ cm^3/s and $C \approx 8.1 \times 10^{-29}$ cm^6/s [21], leading to $\eta_r \approx 0.46$. According to the model,

$$\Phi_{G,\text{tot}} = \int_{z_{\min}}^{z_{\max}} (G_{IT} + G_{II}) dz, \qquad (6)$$

where G_{IT} is the generation rate associated with interband tunneling, G_{II} is the generation rate associated with impact ionization, and $z_{\min}$ to $z_{\max}$ defines the range on the collector side where there is significant electron-hole generation. As we will see below, both $z_{\min}$ and $z_{\max}$ depend on the mechanism.

For this analysis, we first need an accurate evaluation of band bending in the device under bias. A representative plot of the electron's potential energy is shown in Fig. 7 at $V_B = 2.9$ V, as derived from a numerical computation that connects a self-consistent Poisson-Schrödinger equation
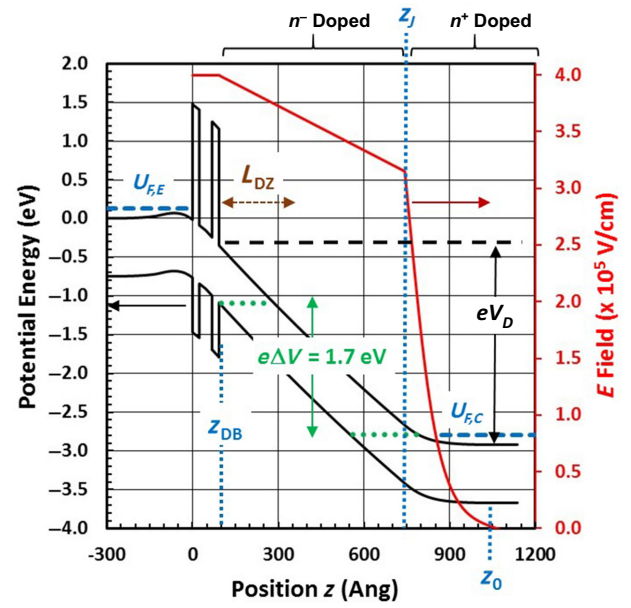

FIG. 7. Computed band bending (left vertical axis) and internal electric field (right vertical axis) for the qualitative models shown in Fig. 6 and a bias voltage of 2.9 V. Also shown is the energy range, $\Delta E = e\Delta V$ ("tunneling window"), over which interband tunneling can occur in the high-field region on the collector side.

solver on the emitter side to a Poisson solver on the collector side, both using the second-order Unger approximation for (degenerate) free-electron density [22]. No accumulation of electrons is assumed to occur in the quantum well, which is a reasonable approximation when a double-barrier RTD is biased above the peak voltage at $V_B = 1.8$ V for the present device.

The band-bending plot of Fig. 7 shows that, as might be expected, the majority of the bias voltage drops across the collector side, creating a high-field region that extends over the entire 65-nm n^--doped ($N_D = 1 \times 10^{17}$ cm^{-3}) area on this side and partially into the n^+-doped region outside it. It also shows the magnitude of the internal electric field, $E(z)$, obtained from $E(z) = |d\phi/dz|$, where ϕ is the electrostatic potential. $E(z)$ is the most-important physical quantity in interband tunneling and is similarly important for impact ionization. In the present structure, E has a maximum value, $E_{\max}$, at the boundary between the double-barrier structure and the n-doped region, which remains true, even if there is some electron accumulation in the quantum well. On the collector side, $E(z)$ decreases gradually across the low-doped region and then rapidly at the n^--n^+ homojunction shown at $z = z_J$ in Fig. 7. It then falls to zero at $z = z_0$, which occurs about 30 nm beyond z_J at 2.9 V, but less beyond z_J at lower bias. The small drop in E of only about 25% across the n^--doped region is important, since this helps to justify the transport analysis given below.

Generation of holes by interband tunneling.—To obtain the interband tunneling *available* hole flux, $\Phi_{G,\mathrm{IT}}$, we must apply an expression for G_{IT} and then integrate it across the high-field region while being careful to include only z values that lie within the tunneling "window," i.e., connect a valence-band state to an unoccupied conduction-band state at the same energy. Figure 7 depicts this tunneling window and the associated z locations at $V_B = 2.9$ V; z_{DB} is the collector-side edge of the double-barrier structure and $z_{\max}$ is the furthest point in the high-field region where elastic tunneling can occur. Using the expression for G_{IT} described in Appendix C, we obtain

$$\Phi_{G,\mathrm{IT}} = \int_{z=z_{\mathrm{DB}}}^{z_{\max}} G_{\mathrm{IT}}\,dz = \frac{2^{1/2}}{4\pi^3}\left(\frac{e}{\hbar}\right)^2\left(\frac{m_r}{U_G}\right)^{1/2}$$
$$\times \int_{z=z_{\mathrm{DB}}}^{z_{\max}} E^2(z)\exp\left[\frac{-\pi m_r^{1/2} U_G^{3/2}}{2^{3/2} e\hbar E(z)}\right]dz. \quad (7)$$

In our device at $V_B > {\sim}1.0$ V, the tunneling window is approximately $\Delta V \approx V_C - (U_G - U_{F,C})/e$, where V_C is the voltage drop across the collector side and $U_{F,C}$ is the Fermi energy in the n^+ region on the collector side ($U_{F,C} \approx 0.131$ eV for $N_D = 2 \times 10^{18}$ cm^{-3} at 300 K). Then $z_{\max}$ is calculated from $z_{\max} \approx z_{\mathrm{DB}} + \Delta V/\bar{E}$, where $\bar{E} \equiv \int_{z_{\mathrm{DB}}}^{z_0} E(z)\,dz$ is the average across the high-field n^--doped region over which $|E| > 0$. For example, Fig. 7 shows that at $V_B = 2.9$ V, $V_C \approx 2.6$ V, $\Delta V = 1.7$ V, and $\bar{E} = 3.6 \times 10^5$ V/cm, $z_{\max} = 56$ nm.

Given these conditions, we compute the available interband-tunneling current, $e\Phi_{G,\mathrm{IT}}$, from Eq. (7), and the corresponding band-bending diagram is computed in steps of 0.1 V for V_B between 1.0 and 3.0 V. This includes the additional relation $V_C = V_B - V_W - V_E$, where V_W and V_E are the voltage drops across the double-barrier structure and the emitter side, respectively. The resulting plot of $e\Phi_{G,\mathrm{IT}}$ versus V_B is shown in Fig. 8, along with the light-emission curve of Fig. 2 (right-hand axis of Fig. 8). The interband-tunneling curve mimics the most important and practical aspect of the light-emission behavior, which is the steep rise in photocurrent between about 2.5 and 3.0 V beyond the valley point. In this same range of bias, the RTD electric current is increasing much more slowly, suggesting that light emission in this bias region is *field driven*, which is consistent with interband tunneling, but perhaps impact ionization as well, as addressed next.

Generation of holes by impact ionization.—The other likely hole-generation mechanism in our device is impact ionization, which has been studied continuously in In$_{0.53}$Ga$_{0.47}$As devices for several decades. Much of the interest has stemmed from making high-performance high-speed In$_{0.53}$Ga$_{0.47}$As *p-i-n* photodiodes for 1550-nm fiber telecommunications, In$_{0.53}$Ga$_{0.47}$As avalanche photodiodes for low-light sensing, or InP-based high-speed and
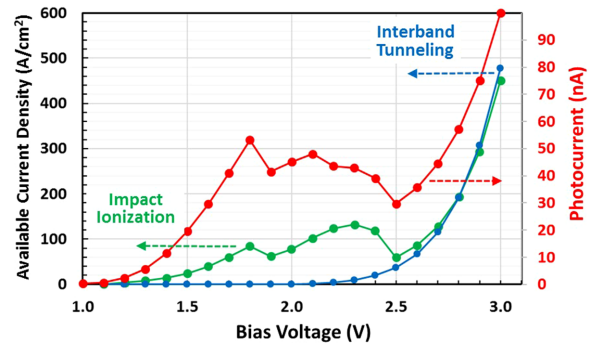

FIG. 8. Computed available current density for interband tunneling and impact ionization (left vertical axis) in comparison to photocurrent (right vertical axis). Interband-tunneling curve assumes $U_G = 0.747$ eV and $m_r = 0.023\,m_e$. Impact-ionization curve assumes electron-ionization coefficients from Fig. 9.

low-noise transistors (HBTs and HEMTs) for analog and digital signal processing. It has been known since the early days of semiconductor devices that modeling impact ionization and distinguishing it from interband tunneling is tricky. Fortunately, the essential physical quantities to estimate the degree of hole generation—the electron and hole ionization coefficients defined here as α and β, respectively—have been derived by several researchers from both HBT and *p-i-n* photodiode measurements. Perhaps the most-reliable method, involving calibrated photoexcitation of *p-i-n* photodiodes, has resulted in the threefold piecewise-continuous expressions for α tabulated in Fig. 9(a) and applicable at room temperature (300 K) up to an E field of 3×10^5 V/cm [23]. Above this value, we carry out an extrapolation of region III up to $E = 5 \times 10^5$ V/cm to define region IV, which is based on results from Monte-Carlo simulations [24]. This yields the traditional plot of α versus $1/E$ shown in Fig. 9(b). A similar curve can be constructed for β but in In$_{0.53}$Ga$_{0.47}$As it is significantly smaller than α (e.g., $\alpha \approx 5 \times \beta$ at $E = 3 \times 10^5$ V/cm [23]). We expect these ionization coefficients to be applicable to both the resonant, J_R, and nonresonant, J_{NR}, tunneling current components of Fig. 6. This assumes that J_R and J_{NR} contain a significant number of electrons that gain enough kinetic energy across the collector side to exceed the impact-ionization threshold.

At high bias, there should be a boundary on the collector side of Fig. 6 beyond which hole generation by impact ionization becomes negligible. For the present analysis based on 2.9-V bias and Fig. 7, we assume this occurs in the n^+ region where the E field approaches zero or at $z \equiv Z_0 \approx 105$ nm. After drifting across the high-field region, electrons will relax very quickly because of the low field, and there will be a large free-electron and ionized-donor density beyond this boundary. Another important aspect is the inclusion of a "dead zone" starting at the double-barrier edge of the high-field region. This is where

(a)

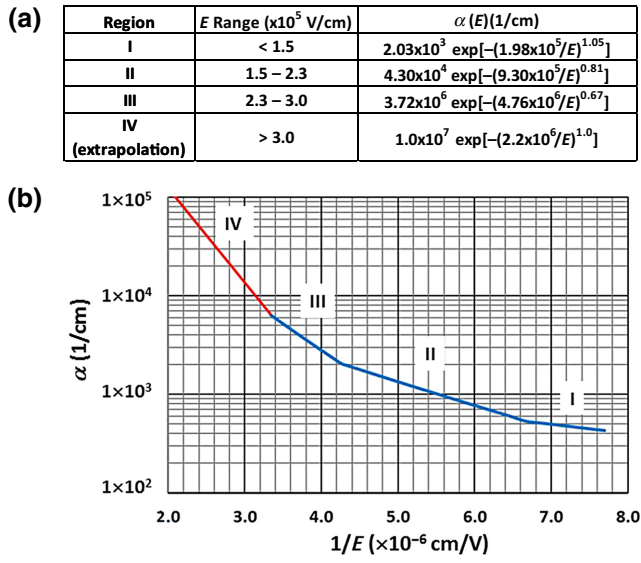| Region	E Range (x10⁵ V/cm)	$\alpha(E)$(1/cm)
I	< 1.5	$2.03 \times 10^3 \exp[-(1.98 \times 10^5/E)^{1.05}]$
II	1.5 – 2.3	$4.30 \times 10^4 \exp[-(9.30 \times 10^5/E)^{0.81}]$
III	2.3 – 3.0	$3.72 \times 10^6 \exp[-(4.76 \times 10^6/E)^{0.67}]$
IV (extrapolation)	> 3.0	$1.0 \times 10^7 \exp[-(2.2 \times 10^6/E)^{1.0}]$

(b)

FIG. 9. (a) Table of expressions for electron impact-ionization coefficient over four contiguous regions of internal electric field. (b) Graphical representation of (a).

the kinetic energy of incoming electrons is below the threshold to induce an impact-ionization event. Although the kinetic energy threshold, U_{th}, is not well defined in $In_{0.53}Ga_{0.47}As$ [24], we can estimate it using the rule of thumb that $U_{th} = 1.5U_G$ based on the conservation of energy and momentum for electrons confined to parabolic conduction bands [25]. This applies to $In_{0.53}Ga_{0.47}As$, at least for sufficiently low kinetic energy electrons. Then, given the band bending of Fig. 7, the dead-zone length can be estimated as

$$L_{DZ} \approx 1.5U_G/E_{max}, \qquad (8)$$

where E_{max} is the maximum electric field at the edge of the double-barrier structure, which is about 4.0×10^5 V/cm at $V_B = 2.9$ V. This corresponds to $L_{DZ} \approx 28$ nm and, at lower bias, L_{DZ} will be even longer.

As with interband tunneling, we require an expression for the impact-ionization available hole flux, $\Phi_{G,II}$, obtained by integrating the generation rate, G_{II}, with respect to z. As derived in Appendix D, a simple but plausible approximation for G_{II} leads to

$$\Phi_{G,II} = \int_{z_{min}}^{z_{max}} G_{II} dz \approx (J_T/e) \int_{z_{DZ}}^{z_0} \alpha(z) dz. \qquad (9)$$

Using the piecewise-continuous expressions for $\alpha(E)$ in Fig. 9(a), this allows a numerical integration of Eq. (9), which is carried out between $V_B = 1.0$ and 3.0 V in 0.1 V steps. The result is plotted in Fig. 8 as an *available* impact-ionization current in direct comparison with the interband-tunneling component. Clearly, the impact-ionization current dominates at lower bias voltages, but beyond the

valley point becomes comparable to the interband current, which rises faster with bias voltage. Nevertheless, both mechanisms mimic the behavior of the photocurrent in this bias region in that both rise much faster with bias than J_T, as shown clearly in Fig. 2. Hence, impact ionization appears to be both *current* and *field driven*; the latter behavior arises from the strongly nonuniform behavior of α versus $1/E$ shown in Fig. 9(b).

Charge-transport IQE versus bias voltage.—Given the above analysis, we can construct the plot of Eq. (4) versus V_B shown in Fig. 10(a) with the $e\Phi_{G,IT}$ and $e\Phi_{G,II}$ functions plotted individually and in total, along with the value of $\eta_r \approx 0.46$ [from Eq. (5)] and the values of the terminal electric current density, J_T, from Fig. 2. Also displayed for comparison is the IQE curve for the radiometric calculation from Eq. (3) and Fig. 5. A magnification of the high-bias region beyond the valley point is shown in Fig. 10(b), where we see that, at the highest bias voltage of 3.0 V, the charge-transport IQE is about 10% compared to 6% for the radiometric approach. The discrepancy between the two decreases with reduced bias, so at $V_B = 2.7$ V they are practically equal and below that the radiometric IQE exceeds the transport IQE by an amount that increases with decreasing bias.

A related plot and one that serves as a test of our modeling is shown in Fig. 11. It is the ratio of $e\Phi_{G,tot}/J_T = (e\Phi_{G,IT}$ and $e\Phi_{G,II})/J_T$, which, from Eq. (4), is the available injection efficiency, η_i. We see that this
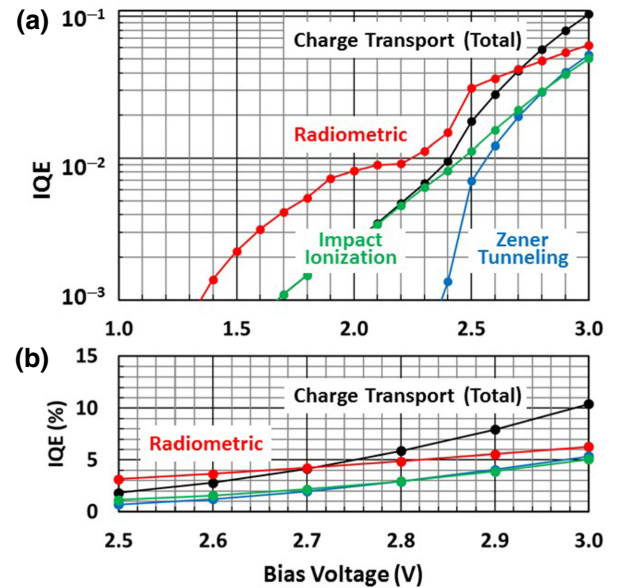

FIG. 10. (a) Internal quantum efficiency computed by radiometric and charge-transport approaches, showing the individual contributions by interband tunneling and impact ionization to the charge-transport approach. (b) Magnification of the high-bias region of (a) and plotted on a linear scale.
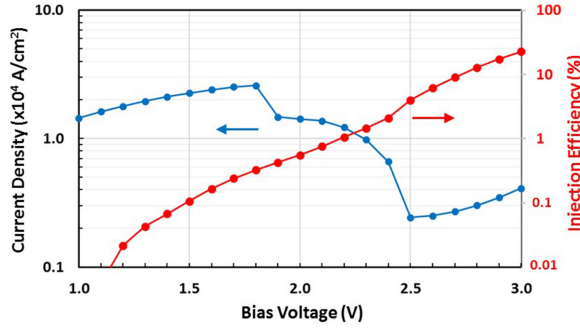
FIG. 11. Terminal electric current (from Fig. 2) and available injection efficiency (right vertical axis).

increases very rapidly with bias voltage, which is consistent with the exponential nature of both the interband-tunneling and impact-ionization mechanisms. At the highest $V_B = 3.0$ V, it reaches about 22%. Although not negligible, as assumed in the development of Eq. (9), it does support the statement that the generation of holes by impact ionization is primarily associated with the non-resonant electron current through the double-barrier structure (J_{NR} in Fig. 6) at bias voltages beyond the valley point.

IV. DISCUSSION

A. Comparison of IQEs

In the bias region above the valley point, the radiometric and charge-transport IQEs agree favorably with the charge-transport IQE increasing faster but equaling the radiometric value at 2.7 V and exceeding it by only 67% at 3.0 V. This supports our transport model of Fig. 6 and suggests that both interband tunneling and impact ionization play a role in hole generation necessary for light emission. However, it has a more profound implication based on the fact that $e\Phi_{IT}$ and $e\Phi_{II}$ are only *available* current densities, but not necessarily electric current densities flowing in the recombination regions on the emitter or collector sides. So, the near equality of the IQEs suggests that the fraction of generated hole current that transfers to the recombination regions is large. For the diffusion process to the quasi-neutral region on the collector side, this is understandable since there is no barrier. However, at the high-bias fields that exist above the valley-point bias, we expect drift ("uphill") to be predominant over diffusion ("downhill"), so the double-barrier structure serves as a bottleneck. Hence, the transfer efficiency of holes through the double-barrier structure must be significantly high. Because holes have much poorer transport than electrons in In$_{0.53}$Ga$_{0.47}$As, this may be surprising. However, given the relatively narrow In$_{0.53}$Ga$_{0.47}$As quantum well and the thin AlAs barriers, the hole quasi-bound states should be well defined such that hole resonant tunneling

may be likely. Also, the AlAs Γ-point barrier height for holes (≈ 0.71 eV) is considerably lower than for electrons (≈ 1.50 eV) (Appendix A). And the spatial quantization in the In$_{0.53}$Ga$_{0.47}$As well splits the valence-band degeneracy according to heavy-hole and light-hole effective masses, creating a multiply resonant transmission. These effects may collectively increase hole transmission, especially for light holes, to a value comparable to electron transmission.

To support these statements, Appendix A summarizes a computation of the electron, light-hole, and heavy-hole transmission probabilities through our double-barrier structure at zero bias carried out by the transfer-matrix method assuming coherent tunneling through the entire structure. The results are plotted in Fig. 12 versus electron and hole incident kinetic energy relative to their respective band edges. Up to 0.30-eV incident energy, the electron and light hole each show one sharp resonance (EL1 and LH1) with a peak transmission of 1.0 (as expected for any symmetric double-barrier structure) and peak energies (quasi-bound level) of 0.193 and 0.183 eV, respectively. Importantly, the light-hole resonance is much broader than the electron resonance. A magnification around the two peaks carried out separately shows that the FWHM is about 0.4 meV for electron resonance and 1.1 meV for light-hole resonance. This can be attributed mostly to the lower Γ-point AlAs barrier height for light holes. Since the electric current through a double-barrier structure is generally proportional to the width of the transmission curve, these results also suggest that light holes can contribute to an electric current density similar to, if not greater than, electrons, if all other factors (such as quasi-Fermi levels) are comparable. This ignores the effect of bias electric field, which always drops the peak transmission below unity and distorts the resonance curve. However, this effect should be practically the same for holes and electrons, since they share the same double-barrier structure, making the current-density comparison bias independent. Note also that Fig. 12 shows three heavy-hole resonances (HH1, HH2, and HH3) peaked at 0.027, 0.107, and 0.236 eV, but they are all much narrower than those of the electron and light hole, so not as likely to support coherent resonant tunneling, although they affect the light-hole–heavy-hole mixing, as mentioned in Appendix A.

The difference in bias dependence of the two IQEs is also an important observation that we have considered but not yet fully analyzed. The $e\Phi_{G,IT}$ and $e\Phi_{G,II}$ *available* current densities of the charge-transport IQE are both strongly dependent on band bending, as displayed in Fig. 7 at 2.9 V. However, this band-bending profile does not account for hole accumulation in the high-field region on the collector side, especially accumulation of holes that are blocked by the double-barrier structure. This will tend to screen the electric field in this region, causing a more rapid fall with z than that displayed by Fig. 7 and a
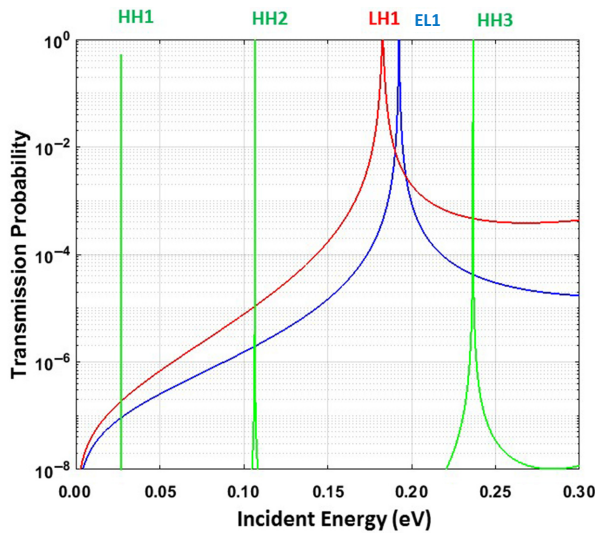
FIG. 12. Transmission probability for electrons (EL), light holes (LH), and heavy holes (HH) through the $In_{0.53}Ga_{0.47}As$ /AlAs double-barrier structure at zero bias, by a computation described in Appendix A.

reduction in the interband-tunneling and impact-ionization hole generation. However, there are two mechanisms that can counteract this effect. The first and most likely is the resonant tunneling of holes to the emitter side, as described above. Just as with electrons, the hole current density should also increase with bias voltage up to a peak-current condition, which occurs roughly when the light-hole quasi-bound level raises above the valence-band edge on the collector side. A second possible counteractive mechanism is electron-hole recombination. Radiative recombination seems unlikely, since at high bias the electrons are depleted from the hole-accumulation region. However, the holes are only separated by 8.4 nm (width of the double-barrier structure) from a strong accumulation of electrons on the emitter side, so nonradiative mechanisms via inelastic tunneling are possible. In any case, a steady state should be reached, and the device should be stable. Furthermore, hole accumulation will introduce a minority-carrier diffusion capacitance, which must ultimately be understood to predict the speed capability of RTD light emitters.

The discrepancy between the radiometric and charge-transport IQEs in Fig. 10(a) at low bias (below the peak voltage of 1.8 V) is about a factor of 4, meaning that our charge-transport model must be inaccurate in this region. In reports of light emission in n-GaAs RTDs, it is proposed that the elastic resonant-tunneling current (J_R in Fig. 6) is very efficient at generating impact ionization on the collector side because of its coherent ballistic nature. While first observed at low temperature [26], it has more recently been observed up to room temperature [27,28]; in all cases, this is attributed to impact ionization. This mechanism should also be present in our $In_{0.53}Ga_{0.47}As$

device, maybe even stronger than in GaAs because of the lower band gap and higher mobility in the $In_{0.53}Ga_{0.47}As$. Intuitively, its effect would be to increase the electron impact-ionization coefficient, α, even higher than the values shown in region IV of Fig. 9. However, the physical analysis, so far, is based on the generalized Keldysh model with only qualitative fitting to data, not the quantitative fitting made possible by impact-ionization coefficients and followed in the present work. None of these references have considered the interband-tunneling mechanism. Furthermore, since the light-emission performance is best in the bias region beyond the valley point, where the α values of Fig. 9 should apply, we do not pursue this methodology in the present work.

B. Design issues

Finally, there is the open question of whether the RTD's light-emission performance can be made more efficient than the 6% IQE value reported here. First, the double-barrier RTD structure should be made with a quantum well that is unusually narrow by RTD electronic device standards. High-speed RTDs are generally designed with a quantum-well width having a ground-state energy of $U_{1,e} \sim 100$ meV. Combined with an n^--layer doping width of about 50–100 nm on the collector side, this usually yields a peak voltage of about 1.0 V and a high peak-to-valley ratio of 10 or higher in high-quality $(In, Ga)As$/AlAs RTDs and 3 or higher in high-quality GaAs/AlAs RTDs, both at room temperature. By contrast, RTD light emitters should be designed with narrower quantum wells to create $U_{1,e}$ approaching 200 meV or above and peak voltages approaching 2.0 V, or above, assuming the PVCR remains high. This is because the electric field across the depleted region on the collector sides increases proportionately to the peak voltage, and both the interband-tunneling and impact-ionization mechanisms are exponentially dependent on the field, albeit in a complicated way.

The second issue is the length and doping concentration of the n^- layer on the collector side. Traditionally, these have been designed with respect to electrical capacitance and carrier transit time. If the n^- layer is too short (at the peak voltage), roughly 50 nm or less, there will be a significant space-charge capacitance under bias that can limit the speed of the device in electronic applications, such as terahertz oscillators and picosecond switches. Similarly, if the n^- layer is too long (at the peak voltage), roughly 100 nm or greater, there will be a significant transit-time delay that could also limit the speed in these applications. For RTD light emitters, at least LEDs, the speed will most likely be limited by the (natural) cross-gap radiative lifetime, in the order of 1 ns, although acceleration effects may be possible. Therefore, to achieve a higher IQE, it would be

prudent to design the n^- region to be longer than that in traditional RTDs and doped to even lower levels, such as the "intrinsic" levels in p-i-n diodes. This will make the electric field more uniform and extend over a greater distance, to enhance both interband tunneling and impact ionization. Of course, this is a delicate business, since both mechanisms can easily lead to device breakdown failure. As n^- increases in length, impact ionization by holes will become significant and add to that by electrons, such that avalanching can occur. However, if breakdown is avoided and the RTD peak-to-valley current ratio remains high, the IQE in the valley region and somewhat beyond could readily exceed the 6% value reported here.

V. CONCLUSION

We carry out spectral and radiometric measurements of the room-temperature electroluminescence from vertically emitting unipolar n-doped $In_{0.53}Ga_{0.47}As$/AlAs RTDs. Emission occurs near the $In_{0.53}Ga_{0.47}As$ band gap and has a peak wavelength consistent with ideal electroluminescence behavior by spontaneous emission and an intensity that increases rapidly with bias voltage beyond the valley point of the RTD. A model is presented that attributes the electroluminescence to electron-hole radiative recombination on the emitter side enabled by hole generation on the collector side and transfer to the emitter side. The EQE is rather low (2×10^{-5}), primarily because of the low optical coupling factor ($\eta_c = 3.4 \times 10^{-4}$); therefore, the radiometric IQE should be much larger and is found to be about 6% at the highest V_B of 3.0 V. An independent charge-transport estimate of the IQE is obtained by separate computation of the available hole current density from the interband-tunneling and impact-ionization mechanisms. This requires an accurate band-bending profile, along with an assumption of Auger-limited nonradiative recombination on the emitter and collector sides. Altogether this enables an independent estimate for IQE of about 10% at $V_B = 3.0$ V. The closeness of the two IQEs suggests that the transport of holes out of the generation region and into the outlying recombination regions is effective, although the balance between recombination on the emitter and collector sides is not yet determined. Our results bode well for the potential application of this *unipolar-doped* RTD-based emission technology in practical photonic source applications (e.g., LEDs), once improvements in the optical external coupling and hole-generation mechanisms are fashioned through improvements in the device design.

Data that support the findings of this study are available within the article.

ACKNOWLEDGMENTS

APPENDIX A

In any heterostructure supporting electron or hole one-dimensional resonant tunneling, it is essential to know the quasi-bound energy levels. This is particularly true in the present $In_{0.53}Ga_{0.47}As$/AlAs double-barrier structure, since electrons are certainly undergoing resonant tunneling and it is likely that holes are too. The first step is establishing the energy bands and band offsets that an electron or hole experience. Since AlAs is a zincblende indirect-band-gap semiconductor with a conduction-band edge at the X point (first Brillouin zone), one might think that the X-point barrier would apply to electrons. However, many years of research on high-speed RTDs with AlAs barriers has shown that the Γ-point barrier in AlAs is most relevant to electron tunneling if the barriers are thin, roughly less than 3.0 nm. The physical argument is that if an electron in the Γ valley of $In_{0.53}Ga_{0.47}As$ tunnels through the AlAs barrier, it will remain in the Γ valley, since tunneling is then elastic, whereas tunneling through the X valley requires phonon interaction, which takes more time than the very short dwell time of an electron in a thin barrier. Given this assumption, we can estimate the electron barrier height from the band offsets. We adopt the same offset rule as for lattice-matched $In_{0.53}Ga_{0.47}As$/$In_{0.52}Al_{0.48}As$ type-I heterojunctions [29], which yields an electron barrier height of $\phi_{B,e} = 0.68\{U_G(\text{AlAs}) - U_G[In_{0.53}Ga_{0.47}As]\} = 1.50$ eV and a hole-barrier height of $\phi_{B,h} = 0.32\{U_G(\text{AlAs}) - U_G(In_{0.53}Ga_{0.47}As)\} = 0.70$ eV, where $U_G(\text{AlAs})$ is the room-temperature Γ-point band gap (≈ 2.95 eV) of AlAs [30] and $U_G(In_{0.53}Ga_{0.47}As)$ is the Γ-point band gap of $In_{0.53}Ga_{0.47}As$ (≈ 0.75 eV) [31]. These offsets are shown in the diagram of Fig. 7. However, this procedure ignores the lateral tensile strain that the thin AlAs barriers undergo when embedded in $In_{0.53}Ga_{0.47}As$, an issue still not fully resolved after 30 years of application.

Given the barrier heights and thicknesses, and the $In_{0.53}Ga_{0.47}As$ well width, the electron and hole ground quasi-bound levels are readily calculated by solving for the transmission probability through the double-barrier structure using the transfer-matrix method [32]. In its simplest form, this method considers only the envelope component of the Bloch function describing each particle and makes the effective mass approximation, a combination that has proven to be useful and accurate in nanoscale heterostructures of many types. By restricting the analysis to electrons, light holes, and heavy holes only (ignoring the split-off band), six effective masses are required. For $In_{0.53}Ga_{0.47}As$, $m^*_e = 0.042\ m_e$, $m^*_{LH} = 0.051\ m_e$, and $m^*_{HH} = 0.457\ m_e$ [31]. For Γ-point AlAs, $m^*_e = 0.146\ m_e$, $m^*_{LH} = 0.15\ m_e$, and $m^*_{HH} = 0.76\ m_e$ [30]. Because the

ground electron level in the well is expected to lie well above the $In_{0.53}Ga_{0.47}As$ band edge and also close to the middle of the AlAs Γ-band gap, two techniques are applied to improve the accuracy. First, band nonparabolicity is included for the well electron using a wave vector, k, consistent with

$$U(k) = \frac{(\hbar k)^2}{2m^*}\left[1 - \alpha\frac{(\hbar k)^2}{2m^*}\right], \qquad (A1)$$

where $\alpha = 1.17$ eV^{-1} is the nonparabolicity parameter [33]. For a given k, Eq. (A1) reduces the energy of the electron in the well compared to the parabolic case. The second technique is to compute the (imaginary) k in the AlAs band gap by analytical continuation of the U versus k relation between the conduction-band edge and the light-hole-band edge [34]. This has the effect of reducing the magnitude of k in the AlAs barrier, particularly near the center of the AlAs band gap, and thus, makes the AlAs barriers appear more transparent to electrons than in the parabolic case.

In contrast, the light and heavy holes are analyzed assuming parabolic U versus k in both the well and AlAs barriers using the appropriate effective mass. This ignores the complicated band mixing that occurs in the valence band of many heterostructures and requires multiband tight binding or $k \cdot p$ methods to treat rigorously. However, it greatly simplifies the computation and in type-*I* double-barrier structures, such as GaAs/(Al, Ga)As and (In, Ga)As/AlAs, still yields close to the rigorously computed quasi-bound energy levels [35]. What changes significantly is the peak of the transmission resonances; the light hole shows much higher transmission in the presence of mixing than for the parabolic case [35]. This further supports the argument that the light-hole transmission probability can be significantly high. The results for our particular double-barrier structure at zero bias are plotted in Fig. 12 and discussed in Sec. IV A.

APPENDIX B

To obtain the charge-transport estimate of the IQE, we start with the fundamental definition applicable to electroluminescence in any vertically oriented solid-state device:

$$\text{IQE} = (\text{internal photon} - \text{generation flux})/$$
$$(\text{total charge} - \text{carrier flux}) \equiv \Phi_{R,R}/\Phi_Q, \quad (B1)$$

where flux has the usual meaning in transport theory (number per unit area $\times$ time) and applies here, assuming all transport mechanisms are uniform across any horizontal plane perpendicular to the electric current flow. For the model of Fig. 6, the internal radiative-recombination flux is just

$$\Phi_{R,R} = \int_E R_R(z)dz + \int_C R_R(z)dz. \qquad (B2)$$

$R_R(z)$ is the spontaneous radiative recombination rate of electron-hole pairs (i.e., "bimolecular"), and E and C denote the emitter and collector sides of the structure, respectively. The integrals are assumed to span far enough along the z axis of the emitter and collector sides to account for all radiative recombination from the device. The total charge-carrier flux is just the terminal current density, J_T, per unit charge, $\Phi_Q = J_T/e$, where J_T for the present device is plotted in Fig. 2. This leads to the compact expression

$$\text{IQE} = e\Phi_{RR}/J_T. \qquad (B3)$$

In competition with the radiative mechanism of Eq. (B2) is nonradiative recombination, for which we can write another flux:

$$\Phi_{R,N} = \int_E R_N(z)dz + \int_C R_N(z)dz, \qquad (B4)$$

where, again, the integrals are assumed to span far enough along z to account for all of the nonradiative recombination. This leads to a total recombination flux:

$$\Phi_{R,\text{tot}} = \Phi_{R,R} + \Phi_{R,N}. \qquad (B5)$$

To proceed further, relationships are needed between $\Phi_{R,\text{tot}}$, $\Phi_{R,R}$, and $\Phi_{R,N}$. According to the model in Fig. 6, all recombination occurs in the n^+ regions on the emitter side and in the quasi-neutral region or beyond on the collector side. For direct-band-gap semiconductors like $In_{0.53}Ga_{0.47}As$, rate-equation analysis commonly used in LED and laser-diode devices defines a (spontaneous) radiative recombination rate of

$$R_R(z) = Bnp, \qquad (B6)$$

where B is the bimolecular recombination coefficient, and n and p are the local electron and hole densities, respectively. In principle, all three of these quantities depend on z. Assuming $n \gg p$, the nonradiative-recombination rate can be estimated through the Auger-recombination expression involving three electrons and one hole (often called CCCH, CHCC, or Auger process no. 1 in the literature):

$$R_N(z) = Cn^2p, \qquad (B7)$$

where C is the associated Auger coefficient. As in Eq. (B6), C, n, and B are inherently functions of z. This leads to a useful expression for the ratio of $\Phi_{R,R}$ to $\Phi_{R,\text{tot}}$

$$\frac{\Phi_{R,R}}{\Phi_{R,\text{tot}}} = \frac{\int_E Bnpdz + \int_C Bnpdz}{\int_E (Bnp + Cn^2p)dz + \int_C (Bnp + Cn^2p)dz}$$
$$\equiv \eta_R. \tag{B8}$$

We can rewrite the IQE from Eq. (B3) compactly as

$$\text{IQE} = e\eta_R\Phi_{R,\text{tot}}/J_T, \tag{B9}$$

where η_R is the radiative-recombination factor. If we now assume that $n(z)$ on both the emitter and collector sides is uniform and equal to the local n^+-donor density, N_D, then B and C will also be uniform on each respective side and we can write

$$\eta_R = \frac{(BN_D)_E \int_E p(z)dz + (BN_D)_C \int_C p(z)\, dz}{(BN_D + CN_D^2)_E \int_E p(z)dz + (BN_D + CN_D^2)_C \int_C p(z)\, dz}. \tag{B10}$$

While, in general, requiring knowledge of the hole spatial density on each side, it has a great simplification in a symmetrically doped structure, where N_D is the same on both sides, leading to

$$\eta_R = \frac{BN_D\left[\int_E p(z)dz + \int_C p(z)\, dz\right]}{(BN_D + CN_D^2)\left[\int_E p(z)dz + \int_C p(z)\, dz\right]} = \frac{BN_D}{BN_D + CN_D^2} = \frac{1}{1 + CN_D/B}, \tag{B11}$$

by cancellation of the hole spatial integrals.

Lastly, according to our model, all of the holes are assumed to be generated in the $E > 0$ region on the collector side and associated with a total generation rate, G_{tot}, and associated flux:

$$\Phi_{G,\text{tot}} = \int_{E>0} G_{\text{tot}}dz\, . \tag{B12}$$

At steady state, the total recombination flux must equal the total generation rate, $\Phi_{R,\text{tot}} = \Phi_{G,\text{tot}}$. Hence, we can rewrite the IQE as

$$\text{IQE} = e\eta_R\Phi_{G,\text{tot}}/J_T \equiv \eta_R\eta_I, \tag{B13}$$

where η_I is the so-called electrical injection efficiency. Remarkably, this expression does not require knowledge of the hole densities in either recombination region.

APPENDIX C

Following Zener's seminal paper, more detailed theoretical work on interband tunneling was carried out in the 1950s and 1960s, first by Keldysh [36] and then by Kane [37,38]. Kane's second paper focused on the general case of interband tunneling across the junction of heavily doped p-n junctions. Here, we apply a simplification of this analysis described succinctly by Moll and applied to the interband-tunneling case between a fully occupied valence and empty conduction bands under the influence of a large internal electric field [25]. For direct narrow-band-gap semiconductors like $\text{In}_{0.53}\text{Ga}_{0.47}\text{As}$, this process

is expected to be elastic, meaning that phonons are not necessary. In analyzing the interband current density across the intrinsic (i) region of a back-biased p-i-n junction, Moll derived an expression for the terminal current that does not apply exactly to our device because of our nonuniform field and the blocking effect of the double-barrier structure. However, it corresponds to the following approximate local generation rate in the high-field region:

$$G_{\text{IT}}(z) \approx \frac{2^{1/2}}{1/4\pi^3}\left(\frac{e}{\hbar}\right)^2 E^2(z)\left(\frac{m_r}{U_G}\right)^{1/2} exp\left[\frac{-\pi m_r^{1/2}U_G^{3/2}}{2^{3/2}e\hbar E(z)}\right], \tag{C1}$$

where $E(z)$ is the local electric field, m_r is the reduced effective mass, and U_G is the band-gap energy. The reduced mass is given by $m_r = (1/m_c + 1/m_v)^{-1}$, where m_c and m_v are the electron and light-hole masses, respectively. This definition is best suited to narrow-band-gap III-V semiconductors, like InSb and InAs, but should be a good approximation for $\text{In}_{0.53}\text{Ga}_{0.47}\text{As}$. The strongest effect on G_{IT} occurs through the $U_G^{3/2}$ and E^{-1} terms in the argument of the exponent. For $\text{In}_{0.53}\text{Ga}_{0.47}\text{As}$, we use the room-temperature values $U_G = 0.747$ eV, $m_c = 0.042\, m_e$, and $m_v = m_{\text{LH}} = 0.051\, m_e$, so that $m_r = 0.023\, m_e$ [31].

APPENDIX D

For semiconductors, there exists the following general expression for the local *current-driven* impact-ionization

generation rate [25]:

$$G_{\mathrm{II}}(z) = (1/e)[\alpha(z)J_N(z) + \beta(z)J_P(z)] = (1/e)dJ_{\mathrm{II}}/dz,$$
$$(D1)$$

where α and β are the electron and hole impact-ionization coefficients, J_N and J_P are the *net* electron and hole electric current densities, and J_{II} is the *available* hole current corresponding to G_{II}. J_N includes contributions from the electron resonant-tunneling current, J_{RT}; the interband-tunneling current, J_{IT}; and the impact-ionization currents, J_{II}, such that $J_N = J_{\mathrm{RT}} + J_{\mathrm{IT}} + J_{\mathrm{II}}$, whereas J_P includes only contributions from J_{IT} and J_{II}. It is understood that Eq. (D1) changes with each bias voltage, and thus, each electric field distribution across the device. However, independent of bias, the steady-state current-continuity relation, $J_N(z) + J_P(z) = J_T$ (a constant), must apply at all z. Hence, we can rewrite (D1) as

$$G_{\mathrm{II}}(z) = (1/e)\{\alpha(z)J_T + [\beta(z) - \alpha(z)]J_P(z)\}. \quad (D2)$$

This rearrangement is motived by the fact that J_T is a known quantity: the total (terminal) electric current density plotted in Fig. 2 for our particular device. An analytical solution to Eq. (D2) is complicated by the fact that $J_P(z)$ includes both the interband-tunneling and impact-ionization mechanisms, which have different spatial dependencies in our structure, as discussed above for our electroluminescence model of Fig. 6. The interband mechanism should generate the most holes between $z = z_{\mathrm{DB}}$ and $z \approx z_J$, where, as shown in Fig. 7, the E field is the strongest. The impact ionization should generate the most holes between $z = z_{\mathrm{DZ}}$ and z_0, where the electrons should have their highest kinetic energy. To alleviate this complexity, we take advantage of the simplification that occurs when the second term of Eq. (D2) is negligible compared to the first term. This happens naturally when $\alpha(z) \approx \beta(z)$, as occurs in semiconductors like GaAs and Si at high fields. But, as described above, this it is not so true in $\mathrm{In}_{0.53}\mathrm{Ga}_{0.47}\mathrm{As}$. So, instead, we assume simply that $J_P(z)$ is $\ll J_T$ at all z, which allows us to immediately rewrite Eq. (D2):

$$G_{\mathrm{II}} \approx (J_T/e)\alpha(z). \quad (D3)$$

[1] C. Zener, A theory of the electrical breakdown in solid dielectrics, Proc. R. Soc. London, Ser. A **145**, 523 (1934).

[2] L. Esaki, New phenomenon in narrow germanium p-n junctions, Phys. Rev. **109**, 603 (1958).

[3] W. Hansch, C. Fink, J. Schulze, and I. Eisele, A vertical MOS-gated Esaki tunneliing transistor in silicon, Thin Solid Films **369**, 387 (2000).

[4] P. M. Solomon, J. Jopling, D. J. Frank, C. D'Emic, O. Dokumaci, P. Ronsheim, and W. E. Haensch, Universal tunneling behavior in technologically relevant P/N diodes, J. Appl. Phys. **95**, 5800 (2004).

[5] A. C. Seabaugh and Q. Zhang, Low voltage tunnel transistors for beyond CMOS logic, Proc. IEEE **98**, 2095 (2010).

[6] G. Dewey, B. Chu-Kung, R. Kotlyar, M. Metz, N. Mukherjee, and M. Radosavljevic, *Symposium on VLSI Technology Digest of Technical Papers* (IEEE, Piscataway, NJ, 2012), pp. 45–46.

[7] J. N. Schulman and D. H. Chow, Sb-heterostructures interband backward diodes, IEEE Electron Dev. Lett. **21**, 353 (2000).

[8] R. R. King, D. C. Law, K. M. Edmondson, C. M. Fetzer, G. S. Kinsey, H. Yoon, R. A. Sherif, and N. H. Karam, 40% efficient metamorphic GaInP/GaInAs/Ge multijunction solar cells, Appl. Phys. Lett. **90**, 183516 (2007).

[9] H. I. Cantu, B. Romeira, A. E. Kelly, C. N. Ironside, and J. M. L. Figueiredo, Resonant tunneling diode optoelectronic circuits applications in radio-over-fiber networks, IEEE Trans. Microwave Theory Tech. **60**, 2903 (2012).

[10] R. M. Lewis, H. P. Wei, S. Y. Lin, and J. F. Klem, Effects of prewells on transport in p-type resonant tunneling diodes, Appl. Phys. Lett. **77**, 2722 (2000).

[11] T. A. Growden, W. Zhang, E. R. Brown, D. F. Storm, D. J. Meyer, and P. R. Berger, Near-UV electroluminescence in unipolar-doped, bipolar-tunneling GaN/AlN Heterostructures, Nat. Light: Sci. Appl. **7**, 17150 (2018).

[12] E. R. Brown, W-D. Zhang, T. A. Growden, P. R. Berger, R. Droopad, "Strong Band-Edge Light Emission from InGaAs RTDs: Evidence for the Universal Nature of Resonant- and Zener-Co-Tunneling," arXiv 1804.07666 (2018).

[13] M. Feiginov, C. Sydlo, O. Cojocari, and P. Meissner, Resonant-tunnelling-diode oscillators operating at frequencies above 1.1 THz, Appl. Phys. Lett. **99**, 233506 (2011).

[14] E. R Brown, J. R. Söderström, C. D. Parker, L. J. Mahoney, K. M. Molvar, and T. C. McGill, Oscillations up to 712 GHz in InAs/AlSb Resonant-tunneling diodes, Appl. Phys. Lett. **58**, 2291 (1991).

[15] 5 Stellarnet, Inc. "DWARF-Star" NIR spectrometer, www.stellarnet.us

[16] D. K. Gaskill and N. Bottka, Band-gap determination by photoreflectance of InGaAs and InAlAs lattice matched to InP, Appl. Phys. Lett. **56**, 1269 (1990).

[17] E. F. Schubert, *Light-Emitting Diodes*, 2nd ed. (Cambridge Univ. Press, Cambridge, 2006).

[18] www.thorlabs.com: LED partnumbers 1600L and 1600P.

[19] I. Moreno and C. C. Sun, Modeling the radiation pattern of LEDs, Optics Express **16**, 1808 (2008).

[20] E. R. Brown, W. Zhang, P. Fakhimi, T. A. Growden, and P. R. Berger, *Proceedings of the 2020 Device Research Conference (DRC)* (IEEE, Piscataway, NJ, 2020), pp. 1–2.

[21] R. K. Ahrenkiel, R. Ellingson, S. Johnston, and M. Wanlass, Recombination lifetime of In 0.53 Ga0.47As As a function of doping density, Appl. Phys. Lett. **72**, 3470 (1998).

[22] K. Unger, Reversible formulae to approximate Fermi integrals, Phys. Status Solidi B **149**, K141 (1988).

[23] J. S. Ng, C. H. Tan, J. P. R. David, G. Hill, and G. J. Rees, Field dependence of impact ionization coefficients in In0.53Ga0.47As, IEEE Trans. Electron Dev. **50**, 901 (2003).

[24] J. Bude and K. Hess, Thresholds of impact ionization in semiconductors, J. Appl. Phys. **72,** 3554 (1992).

[25] J. Moll, *Physics of Semiconductors* (McGraw-Hill, New York, 1964).

[26] C. R. H. White, M. S. Skolnick, L. Eaves, and M. L. Lead-beater, Electroluminescence and impact ionization phenomena in a double-barrier resonant tunneling structure, Appl. Phys. Lett. **58,** 1164 (1991).

[27] F. Hartmann, A. Pfenning, M. Rebello Sousa Dias, F. Langer, S. Höfling, M. Kamp, L. Worschech, L. K. Castelano, G. E. Marques, and V. Lopez-Richard, Temperature tuning from direct to inverted bistable electroluminescence in resonant tunneling diodes, J. Appl. Phys. **122,** 154502 (2017).

[28] C. de Oliveira, A. Pfenning, E. D. Guarin, M. D. Teodoro, E. C. dos Santos, V. Lopez-Richard, G. E. Marques, L. Worschech, F. Hartmann, and S. Höfling, Electroluminescence of-off ratio control of n-i-n GaAs/AlGaAs-based resonant tunneling structures, Phys. Rev. B **98,** 075302 (2018).

[29] W. R. Frensley, in *Heterostructure and Quantum Devices*, edited by N. G. Einspruch, W. R. Frensley (Academic, Orlando, 1994), Chap. 1.

[30] S. Adachi, *Physical Properties of III-V Semiconductor Compounds* (John Wiley, New York, 1992).

[31] Y. A. Goldberg and N. M. Schmidt, in *Ternary And Quaternary III-V Compounds*, edited by M. Levinshtein, S. Rumyantsev, M. Shur (World Scientific, Singapore, 1999), Vol. 2.

[32] B. Ricco and M. Y. Azbel, Physics of resonant tunneling. The one-dimensional double-barrier case, Phys. Rev. B **29,** 1970 (1984).

[33] K. Seo, M. Heiblum, C. M. Knoedler, W.-P. Hong, and P. Bhattacharya, Pseudomorphic InGaAs base ballistic hot-electron device, Appl. Phys. Lett **53,** 1946 (1988).

[34] J. N. Schulman and T. C. McGill, Complex band structure and superlattice electronic states, Phys. Rev. B **23,** 4149 (1981).

[35] M. S. Kiledjian, J. N. Schulman, K. L. Wang, and K. V. Rousseau, Hole and interband resonant tunneling in GaAs/AlGaAs and InAs/GaSb/AlSb tunnel structures, Surface Sci. **267,** 405 (1992).

[36] L. V. Keldysh, Behavior of non-metallic crystals in strong electric fields, Sov. Phys. JETP **6,** 763 (1958).

[37] E. O. Kane, Zener tunneling in semiconductors, J. Phys. Chem. Solids **12,** 181 (1959).

[38] E. O. Kane, Theory of tunneling, J. Appl. Phys. **32,** 83 (1961).